EARTHARXIV PREPRINT

Title:

InSARLite: An Open-Source GUI for Streamlined InSAR Time Series Processing

Authors:

Muhammad Badar Munir [a], Hakan Tanyas [a], Islam Fadel [a], Ling Chang [a], Amira Zaki [a], Ashok Dahal [a], Cees van Westen [a], Serkan Girgin [a]

Affiliations:

[a] Faculty of Geo-Information Science and Earth Observation (ITC), University of Twente, Enschede, the Netherlands

Corresponding authors:

Muhammad Badar Munir (mbadarmunir@gmail.com)

Email addresses and ORCID:

Muhammad Badar Munir / ORCID(s): 0009-0002-1961-1883
Hakan Tanyas / ORCID(s): 0000-0002-0609-2140
Islam Fadel / ORCID(s): 0000-0002-0091-8175
Ling Chang / ORCID(s): 0000-0001-8212-7221
Amira Zaki / ORCID(s): 0000-0001-6254-1548
Ashok Dahal / ORCID(s): 0000-0003-3269-5575
Cees van Westen / ORCID(s): 0000-0002-2992-902X
Serkan Girgin / ORCID(s): 0000-0002-0156-185X

This manuscript is a non-peer-reviewed preprint submitted to EarthArXiv.

This manuscript is currently under review at Applied Computing and Geosciences

Version:
Version 1
March 26, 2026

Abstract

Interferometric Synthetic Aperture Radar (InSAR) is a powerful technique for measuring surface deformation at high spatial resolution over large areas. Despite its demonstrated value across geohazards and Earth-surface processes, broader adoption is often limited by the complexity of end-to-end processing workflows and the technical overhead required to execute them. To reduce this barrier, we present InSARLite, an open-source Python graphical user interface that streamlines Sentinel-1 time-series processing while retaining user control over key processing decisions. InSARLite is designed to cover the complete processing chain, from software installation and project setup to raw SAR data ingestion and deformation time-series products, by wrapping the GMTSAR processing chain and guiding users through a stepwise interface. Rather than fully black-box automation, the workflow is designed to support interactive inspection and parameter selection based on outputs from preceding stages. The software automates routine tasks commonly handled through command-line scripting, including data querying and retrieval, orbit-file acquisition, baseline estimation and network design, interferogram generation, unwrapping, and time-series inversion using Small Baseline Subset approaches. InSARLite also introduces guided decision support features, including master-image selection based on baseline centrality, interactive network inspection and editing, and optional masking through an intuitive interface using mean-correlation thresholds, manual delineation, or a combination of both. Interferograms are unwrapped after defining a correlation threshold and the number of cores while respecting the optional mask if provided, and a user-defined reference point is used to normalize unwrapped interferograms prior to time-series analysis. InSARLite further integrates optional atmospheric correction using the Generic Atmospheric Correction Online Service and supports interactive visualization and export of deformation time series. We demonstrate the capabilities of InSARLite using a fatal rainfall-triggered landslide that occurred on 8 December 2024 in northeastern Türkiye, evaluating whether the failed hillslope exhibited detectable precursory deformation.

Keywords: InSAR, GMTSAR, Automation, GUI, Python, Landslide

1. Introduction

Interferometric Synthetic Aperture Radar (InSAR) enables measurement of surface displacement with high spatial resolution and broad spatial coverage (Meyer et al., 2025; Motagh & Riedel, 2024). As a remote sensing technique, InSAR enables the detection of ground displacement over large spatial extents, making it a crucial tool for understanding various geophysical and environmental processes (Biggs & Wright, 2020; Bürgmann et al., 2000; Lu et al., 2007). Its applications encompass a broad spectrum of disciplines, focusing on surface deformation caused by diverse processes, including both anthropogenic activities (e.g., Haghshenas Haghighi & Motagh, 2019; Xu et al., 2017) and natural phenomena associated with earthquakes (e.g., Jin & Fialko, 2021; Liu et al., 2004; Weiss et al., 2020), land subsidence (e.g., Cigna & Tapete, 2021; Khorrami et al., 2020; Wang et al., 2023), volcanic activity (e.g., Camacho et al., 2018; Chen et al., 2017; Pavez et al., 2006), sinkhole formation (e.g., Kim et al., 2019; Talib et al., 2022), and slow-moving landslides (e.g., Bekaert et al., 2020; He et al., 2024; Sadhasivam et al., 2024; Samsonov et al., 2020).

The increasing availability of SAR data, particularly through satellite missions providing global, systematic coverage, has further expanded the potential of InSAR-based analyses (Costantini et al., 2021; Meyer et al., 2025). The Sentinel-1 mission has been especially transformative by providing frequent acquisitions with free and open access, enabling dense time-series analyses of surface displacement at regional to global scales (Morishita et al., 2020; Torres et al., 2012).

However, despite strong growth in both data availability and methodological development, adoption of InSAR remains uneven worldwide. Based on a Scopus search conducted in May 2024 using “InSAR” and “Interferometric Synthetic Aperture Radar” as search criteria, the research output remains heavily concentrated in a small number of regions (Figure 1). China and the United States lead in contributions, followed by countries such as Italy, Germany, France, and Australia, while many countries, particularly across parts of Africa, South America, and Central Asia, show limited or no InSAR-related research contributions under the applied criteria (Figure 1).

Multiple factors may contribute to this disparity. One important constraint is the expertise and training required to design and execute a complete InSAR workflow, together with access to adequate computational resources (Ansari et al., 2016; Yu et al., 2019; Zaki et al., 2024). A further obstacle is the complexity of processing pipelines and the practical barriers associated with installing, configuring, and running software stacks for time-series analysis,

especially for non-specialists (Hrysiewicz et al., 2023). These challenges can become more pronounced for long time-series analyses and large stacks of acquisitions (Ghorbani et al., 2022).

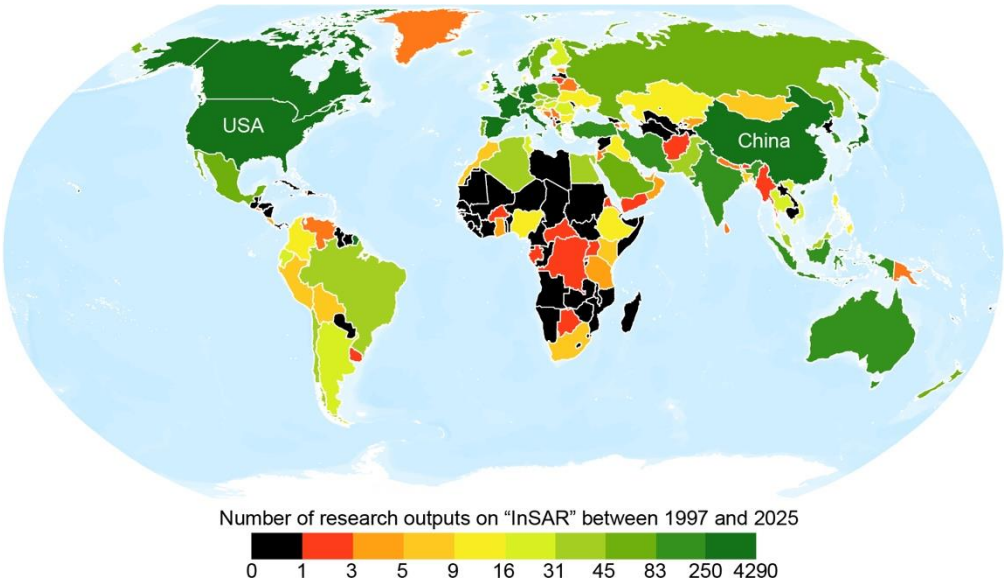

Figure 1: Map showing the number of InSAR-related research publications per country, based on a Scopus search as of May 2024. The counts are derived from author affiliations associated with each country. Data is classified into bins using quantile intervals. Countries with no InSAR-related research under the applied search criteria are shown in black.

While user-friendly software interfaces are available, they are either developed over commercial tools like MATLAB, such as EZ-InSAR (Hrysiewicz et al., 2023) and Kari-MT-InSAR (Lee & Chae, 2024), or are distributed entirely under commercial licenses, such as GAMMA (Wegnüller et al., 2016) or SARscape (Pasquali et al., 2012). The cost of commercial licenses can be prohibitive for many users, particularly in resource-limited settings. Several open-source packages, such as LiCSBAS (Morishita et al., 2020), MintPy (Yunjun et al., 2019), ESA's GUI-based Sentinel Application Platform (SNAP: Zuhlke et al., 2015), DORIS (Calò, 2012), and the Stanford Method for PS (StaMPS; Hooper, 2008), support specific components of InSAR time-series analysis but do not cover the full workflow from raw SAR data to deformation time series. In contrast, software such as GMTSAR (Sandwell et al., 2011), ISCE together with its extensions (e.g., ISCE + MintPy; Gurrola et al., 2010; Yunjun et al., 2019), and SNAP in combination with StaMPS (Hooper, 2008; Zuhlke et al., 2015) are capable of producing deformation time series directly from raw SAR data. Among these, GMTSAR provides a fully integrated environment, whereas ISCE- and SNAP-based approaches typically rely on modular toolchains.

GMTSAR, built around the Generic Mapping Tools (GMT), supports interferogram generation and deformation time-series analysis and provides end-to-end processing capabilities. However, GMTSAR relies heavily on command-line

interface, requiring users to execute and manage Bash or Python scripts to complete the processing pipeline, which can present a substantial usability barrier for users without a strong technical background (Hrysiewicz et al., 2023). To reduce these barriers while leveraging the capabilities of GMTSAR, we developed InSARLite, a front-end, open-source graphical user interface (GUI) that guides users through a complete Sentinel-1 (SLC, IW) time-series workflow. InSARLite is designed to simplify installation and project setup, data querying and acquisition, and core processing while keeping users in control of key processing decisions and parameter choices through a stepwise interface. In addition to streamlining standard GMTSAR operations, InSARLite introduces decision-support functionality that is commonly handled outside a single package. This includes objective master-image selection based on baseline centrality, interactive inspection and editing of the interferometric network with the option to include or exclude interferometric pairs, optional masking to exclude low-coherence areas using mean-correlation thresholds, manual delineation, or a combination of both, and flexible reference-point selection for phase normalization prior to SBAS processing. InSARLite also supports automated requesting of atmospheric correction data and optional correction using the Generic Atmospheric Correction Online Service (GACOS; Yu, Li, & Penna, 2018; Yu, Li, Penna, et al., 2018; Yu et al., 2017), and it provides interactive visualization and export of deformation time series.

A central feature of InSARLite is automation of Small Baseline Subset (SBAS) time-series processing, which is widely used for deformation monitoring (Berardino et al., 2002; Ferretti et al., 2001; Lanari et al., 2007). SBAS exploits a redundant interferogram network and a multi-master strategy to estimate deformation time series, and it can be effective in settings where deformation is spatially distributed and coherence is not restricted to discrete point scatterers. SBAS can incorporate distributed scatterers, often improving performance in heterogeneous terrain (DS; Wang et al., 2012). This makes SBAS particularly useful for geomorphic and landslide applications, where coherent pixels may be spatially extensive rather than isolated (Tong & Schmidt, 2016; Zhao et al., 2012), and it aligns well with the interactive network design and quality-control options implemented in InSARLite.

We demonstrate InSARLite through a case study of a fatal rainfall-triggered landslide at Güngören, northeastern Türkiye, which occurred on 8 December 2024 at approximately 03:05 Türkiye Time (TRT, UTC+3) along the Black Sea coastal road in the vicinity of Araklı, resulting in four fatalities (Gorum et al., 2025). A previous landslide was reported at the same hillslope in 2006, and a technical report on the 2024 event indicated that the hillslope may have shown signs of precursory instability (Gorum et al., 2025). We therefore use this event to illustrate the workflow and to assess whether the failed hillslope exhibited detectable precursory deformation, which would motivate continued

monitoring at the site. By simplifying the workflow and reducing technical overhead, InSARLite aims to make advanced InSAR approaches more accessible to a wider range of users and applications.

2. General overview of InSARLite

We have developed and tested InSARLite in Linux environments and released it as an open-source package via GitHub and PyPI (see the Code Availability section for resources). It primarily uses the Python *"subprocess"* module to orchestrate GMTSAR command-line programs and shell scripts for various processing steps, while replacing selected GMTSAR shell-script components with Python implementations to enhance efficiency and flexibility. The application of Generic Atmospheric Correction Online Service (GACOS) corrections to unwrapped interferograms is one example of this approach. This method builds on the GMTSAR user-contributed shell script (Yu, Li, & Penna, 2018; Yu, Li, Penna, et al., 2018; Yu et al., 2017).

For enhanced performance, we implemented parallel processing using a Python thread pool for several steps that involve repeated execution of similar operations, including GACOS atmospheric correction, interferogram generation, and phase unwrapping. This allows independent jobs to be dispatched concurrently, reducing total processing time for large stacks while preserving the underlying GMTSAR workflow.

InSARLite requires the user's NASA Earthdata credentials to authenticate access to Alaska Satellite Facility (ASF) datasets for different steps of the workflow. These credentials are requested only once and stored locally for automated retrieval in subsequent executions and future runs.

Comprehensive installation instructions, usage, workflow explanations, and detailed function-level documentation elaborating the different interface states are available through the ReadTheDocs platform (https://insarlite.readthedocs.io/). The conceptual structure of InSARLite is organized around four steps (Figure 2).

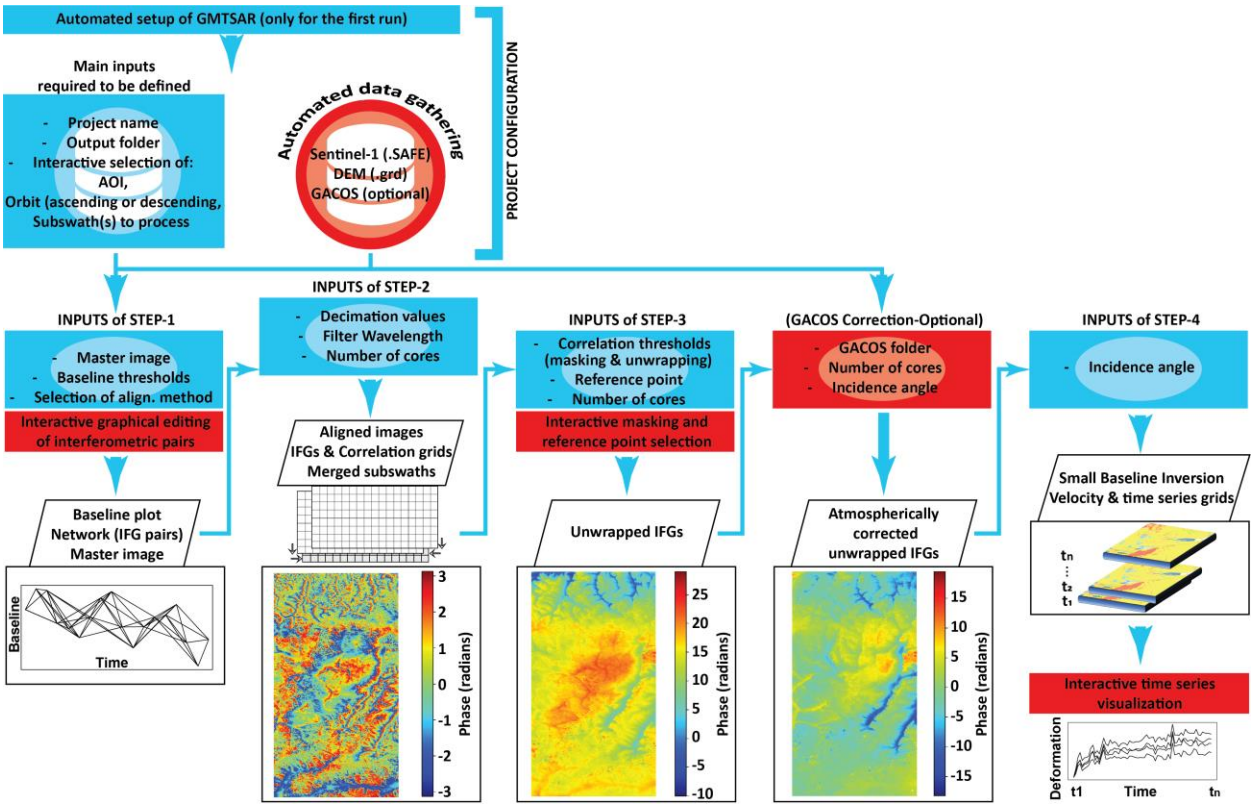

Figure 2: The conceptual structure of InSARLite illustrates four main steps that follow project configuration. The project configuration enables users to define the paths to input datasets of input datasets or to download and/or extract previously downloaded datasets. It also allows users to specify the temporal period, spatial extent and subswath(s), SAR polarization, and orbit direction, setting the foundation for streamlined and automated InSAR time-series processing. Operations highlighted in red indicate newly implemented functionalities within the traditional GMTSAR workflow, while those highlighted in blue represent modifications that support automation and the transition from a command-line interface to a user-friendly interactive interface.

2.1. The Graphical User Interface (GUI)

We structured InSARLite to guide users through the sequential steps of InSAR time-series analysis such that only the controls relevant to the current stage remain active, while other controls are inactive or hidden. Here we present the main interface, the InSARLite Workflow Studio, which is divided into four sub-panels labelled A, B, C, and D (Figure 3). We describe the principal states of each panel without reproducing every intermediate screen for conciseness.

Button controls are color-coded to indicate their status: the default appearance indicates missing the relevant execution/definition of parameter, green indicates readiness for the corresponding action, orange indicates that the action has been partially completed, and red indicates that an optional step has been intentionally skipped.

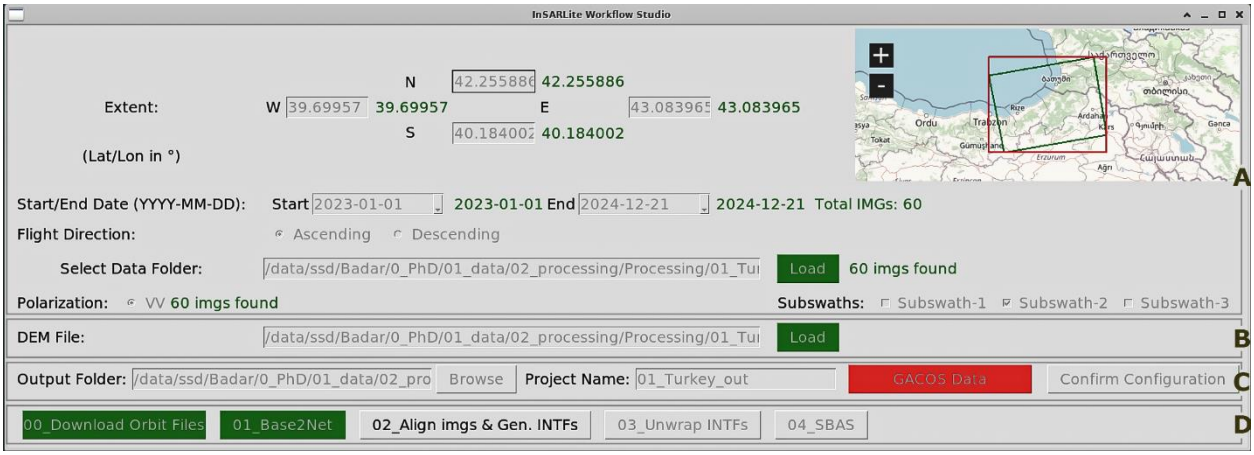

Figure 3: The main graphical user interface, InSARLite Workflow Studio, which manages project configuration by supporting data querying, downloading, and preparation, enabling parameter specification for directory orchestration, and organizing initial input files into the appropriate paths.

Panel A provides controls to define the spatial extent and time period of Sentinel-1 data, and the status of the specified data directory determines the interface state and when subsequent controls become available. If the directory does not exist or is empty, InSARLite keeps all currently visible controls active (except subswath selection) and enables an additional data-query option that returns the top three candidate frames, ranked first by total number of acquisitions and then by percentage coverage; only one frame can be selected at a time. After a successful query, a download button becomes available to retrieve all images for the selected frame, and the relevant download statistics are displayed beneath the map widget. If the specified directory contains zipped downloads, an extraction action becomes available to automate selective data extraction based on user-defined parameters. Once extracted data are present, the remaining controls are unlocked sequentially, following the workflow logic.

Panel B enables Digital Elevation Model (DEM) setup by defining the path of an existing “dem.grd” file or by downloading the required file for the defined project extent automatically. Users can download an SRTM DEM at either 30 m or 90 m resolution using the corresponding download control.

Panel C contains output controls that become available only after a valid DEM has been defined. After specifying the Output Folder and Project Name, InSARLite creates the main project directory and generates the subdirectories and files required for time-series processing.

Panel C also includes an optional GACOS Data button that allows users to configure, prepare, and automatically submit requests for GACOS data with a single action; the request is prepared and submitted for delivery to the specified email address.

GACOS, freely available at http://www.gacos.net/, provides high-resolution tropospheric delay corrections derived from numerical weather models and GPS observations (Yu, Li, & Penna, 2018; Yu, Li, Penna, et al., 2018; Yu et al., 2017). If a path, to already downloaded and extracted GACOS data is specified, the corresponding control is marked as completed.

The Confirm Configuration button deactivates the preceding configuration controls, finalizes the setup, and generates the complete directory structure. Once confirmed, the controls for time-series analysis become accessible.

Panel D contains five buttons related to time-series analysis. The first button performs a final preprocessing step after project configuration, including download of precise Sentinel-1 orbit files, and is therefore labelled with the prefix "00". The four main steps shown in Figure 2 can be executed using the remaining buttons, each labelled with a two-digit integer that corresponds to the step number.

In the following sections, we summarize the principal functionalities of InSARLite and illustrate their application using a case study from Türkiye.

2.2. An InSARLite case study: Güngören, Turkey landslide

For demonstration, we selected the recently documented Güngören landslide, a rainfall-triggered hazard in northeastern Türkiye on 8 December 2024, which exhibited evidence of precursory instability (Gorum et al., 2025). The project configuration shown in Figure 3 aligns with this case study and demonstrates how InSARLite supports an end-to-end workflow, from area selection to stack preparation. The area of interest (AOI) was defined by specifying approximate spatial extents to query and download relevant Sentinel-1 data for the selected temporal window (Figure 3, Panel A) in ascending geometry. In the corresponding map widget, the bounding box of the selected frame (red rectangle) is displayed together with its average footprint (green polygon). We confirmed that the event location is fully covered by subswath IW2 of the frame. Accordingly, we selected only the IW2 subswath for extraction of downloaded data and subsequent analysis. We then used the relevant button to download the precise orbit files for all 60 acquisitions and to prepare the required data.in file, pairing each acquisition with its corresponding orbit file.

Below, we briefly outline the key functionalities available in each of the four time-series analysis steps (sub-GUIs), which are progressively accessible through the corresponding controls.

2.2.1. Step-1: Base2Net

Base2Net comprises four principal actions, with the corresponding controls becoming progressively available in the interface. First, users can select whether processing is performed with or without Enhanced Spectral Diversity (Figure

4, Panel A; ESD; Sandwell et al., 2011). InSARLite then calculates baselines for each input image (Figure 4, Panel B), saves the results as the baseline_table.dat text file, and generates the associated baseline plot, while carrying the selected method forward to the image-alignment step. The metadata of Sentinel-1 SLC IW products provide orbital information and acquisition times, enabling quantification of the spatio-temporal separation between image pairs. In baseline_table.dat, the first acquisition is defined as the reference (zero baseline), and subsequent spatial and temporal separations are computed relative to this image. Spatial baselines are decomposed into parallel and perpendicular components, with the perpendicular baseline being the critical factor influencing interferometric coherence. Temporal baselines are expressed as the number of days elapsed since the first acquisition within the same frame and orbit path (Hooper, 2008; Zebker & Villasenor, 1992). Using these parameters, InSARLite computes the network centrality of each image and generates a ranked list of candidates ordered by optimality (Figure 4, Panel C).

For each candidate master image referred as C and rest of the images as O, the network centrality (labelled as Avg BL in Figure 4, Panel C) is computed as:

$$Network\ Centrality\ (C) = \sum |Baseline(C, O)| \qquad \text{Equation 1}$$

where Baseline(C, O) includes both perpendicular (labelled as Bperp in Figure 4, Panel C) and temporal (labelled as Btemp in Figure 4, Panel C) components:

$$Baseline(C, O) = \left|C_{perp} - O_{perp}\right| + \left|C_{temp} - O_{temp}\right| \qquad \text{Equation 2}$$

We note that some baseline-network ranking methods additionally incorporate Doppler frequency differences as a proxy for acquisition similarity (e.g., Hooper, 2008). Omitting Doppler simplifies the ranking without affecting pair quality for this dataset; we therefore used spatial and temporal baselines alone to compute the ranking. This approach avoids bias introduced by arbitrary reference-scene choices and supports robust master selection for interferometric processing. Third, InSARLite generates an interferometric network that satisfies the user-defined temporal and perpendicular baseline constraints and displays it as an interactive baseline/network plot that can be zoomed and panned (Figure 4, Panel D). Fourth, an Edit Mode (Figure 4, Panel B) allows users to add or remove connections directly within the plotted network.

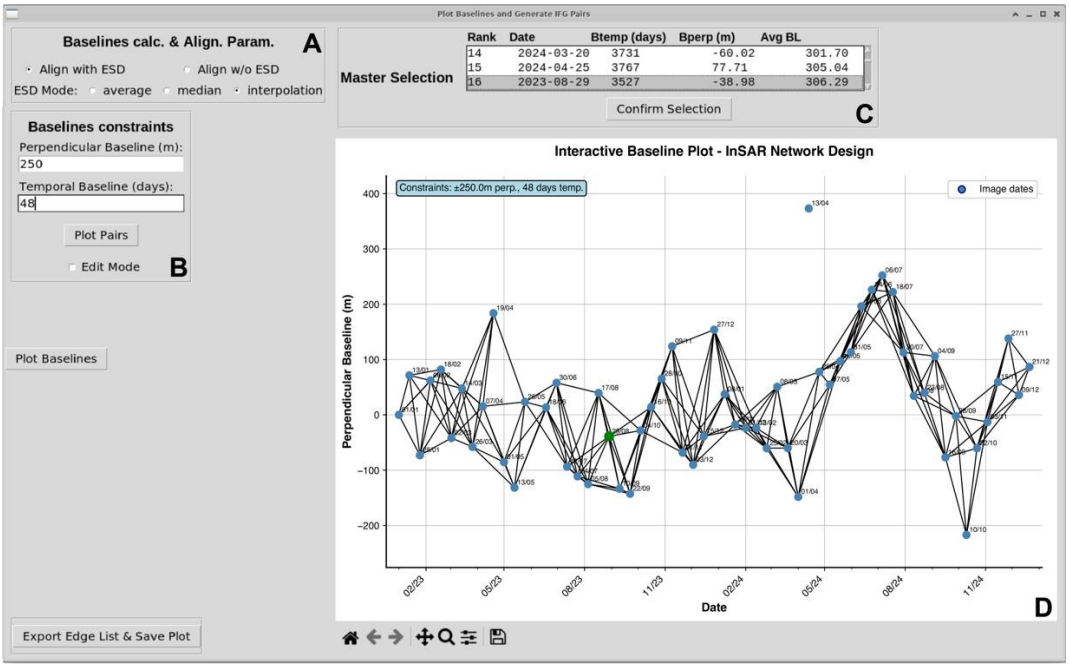

Figure 4: A modified illustration of the Base2Net interface, showing representative states that become available progressively during use. For our study area in Türkiye, we selected a master image acquired on 29 August 2023.

2.2.2. Step 2: Align secondary images and generate interferograms

This step involves defining parameters specific to interferogram generation, including range and azimuth decimation values, filter wavelength, and the number of processing cores (Figure 5a). Execution includes alignment of all images with respect to the selected master, generation of interferograms according to the defined interferometric network, merging of interferograms across subswaths (if multiple subswaths are processed), and calculation of raster layers representing the mean and standard deviation of coherence derived from the correlation grids of individual interferograms (Figure 5b).

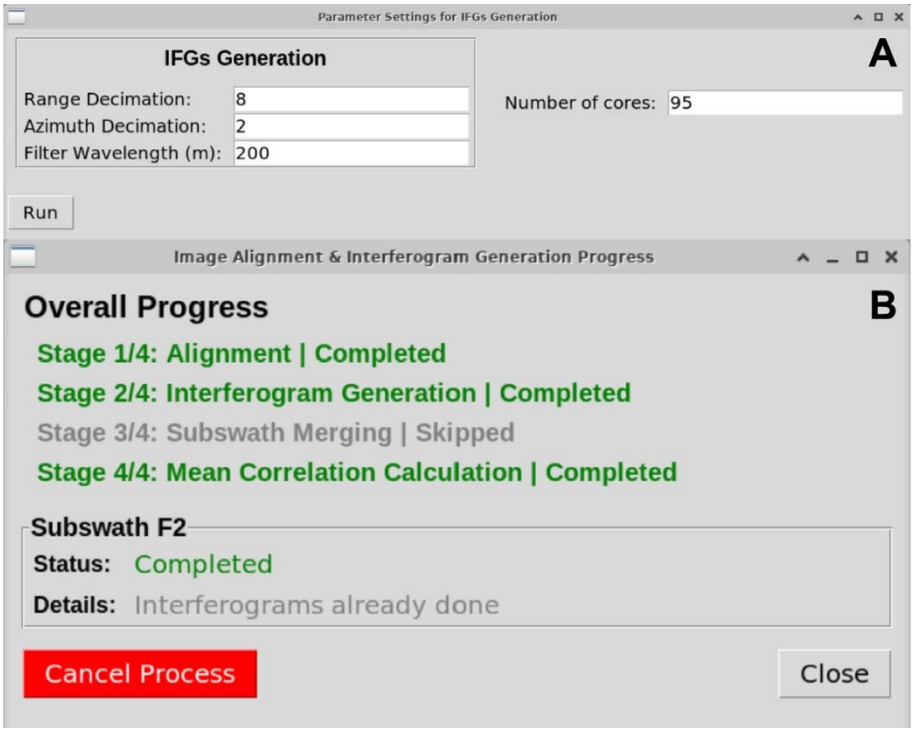

Figure 5: Panels showing (a) the required parameters to initiate interferogram generation and (b) monitoring of related processes, including SAR image alignment, merging of subswaths (if multiple subswaths are processed), and calculation of the mean-correlation grid.

Step 3: Phase unwrapping

This step includes two phases. In the first phase, users can optionally create a mask through an interactive interface using a mean-correlation threshold, manual delineation (by drawing one or more polygons one by one), or a combination of both (Figure 6). All generated interferograms are then unwrapped after specifying a correlation threshold and the number of processing cores, while respecting the optional mask if one is provided.

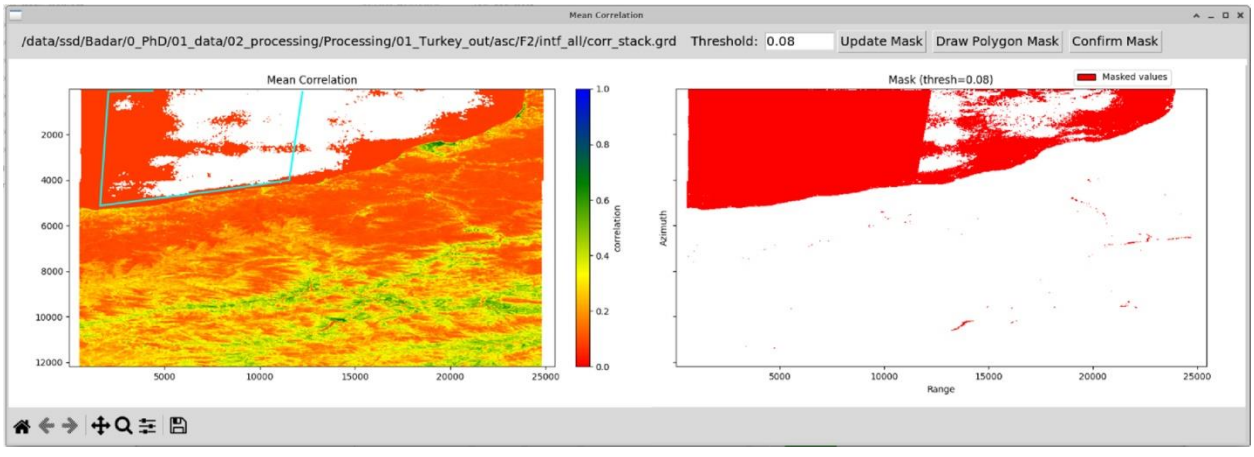

Figure 6: Panels illustrating the interactive mask creation and visualization. For the example shown, we applied a mean-correlation threshold of 0.08 and combined it with manual delineation of a custom polygon (cyan outline in the

left panel) on the mean-correlation map. The resulting mask (right panel) combines the threshold-based and manually delineated components.

In the second phase, users define a reference point to normalize all unwrapped interferograms relative to that location and can optionally apply GACOS atmospheric correction if it was selected during the initial project configuration. Two factors can be considered when selecting the reference point: a high mean correlation and a high validity count. The validity count refers to the number of (unwrapped) interferograms that have a non-null value at a given grid location. A pixel may exhibit high mean correlation but a low validity count; in such cases, normalization relative to that reference point cannot be applied to interferograms in which the reference pixel is null. Users can select the reference point either using automated options (for example, choosing the pixel with the highest mean or the lowest standard deviation of correlation) or through manual selection by inspecting these values, which are displayed in the top-right corner of the panel while hovering the cursor over the study area (Figure 7).

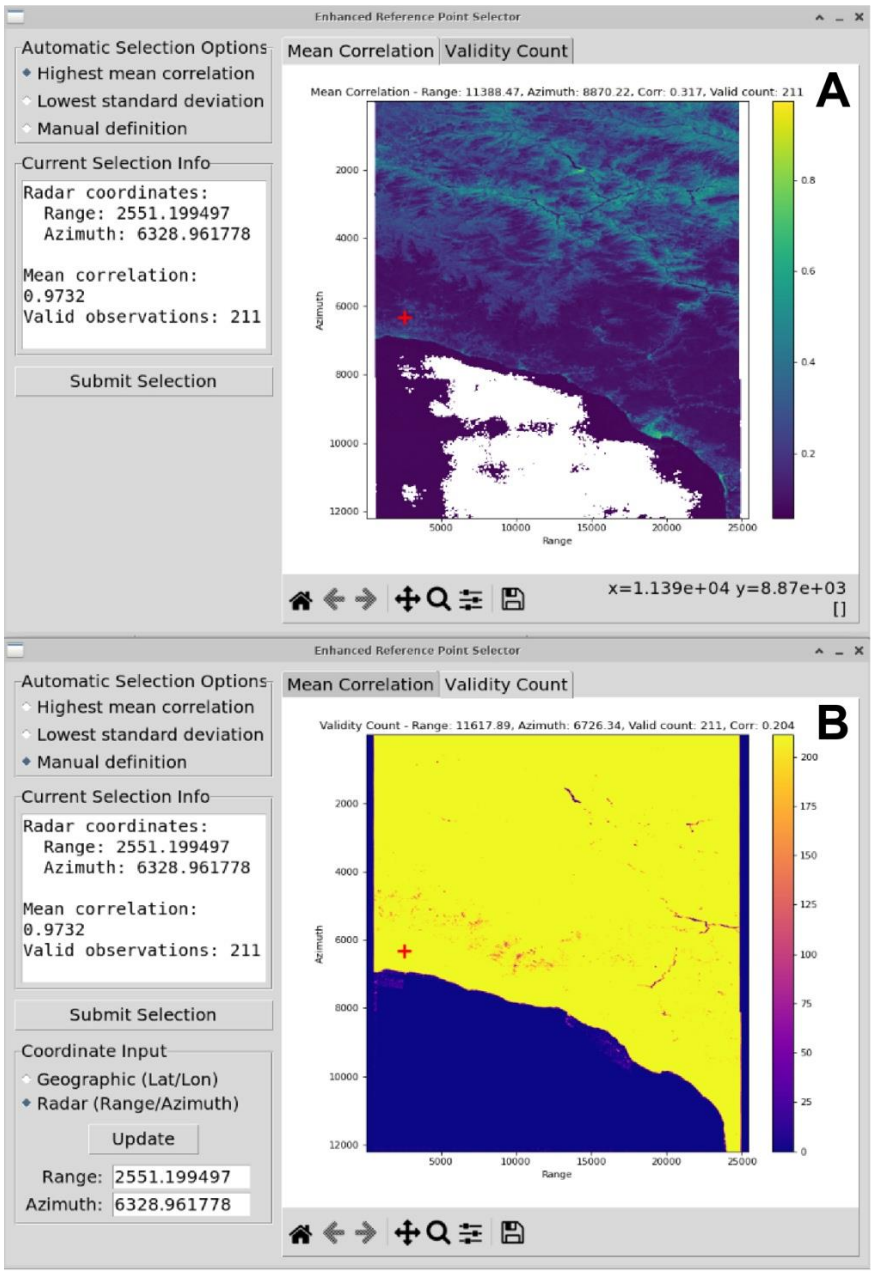

Figure 7: Panels illustrating the available options for reference-point selection: (a) mean-correlation map and (b) validity-count map, with both automated and manual selection options. The selected reference point is indicated by a red plus symbol. The corresponding values are displayed at the top of both maps (Panels a and b) and are also listed on the left side of Panel b. In this menu, both maps are displayed in radar coordinates. For our study area in Türkiye, we selected a reference point at range 2551.199497 and azimuth 6328.961778.

2.2.3. Step-4: SBAS

Small Baseline Subset (SBAS) inversion is the final step in the InSARLite workflow and is performed through SBASApp after specifying the incidence angle, the smoothing factor, the SBAS mode (default SBAS or SBAS Parallel), and optional outputs such as RMS and DEM-residual files (Figure 8a). The workflow also allows an optional

spatio-temporal filtering iteration for atmospheric signal mitigation. Upon successful completion, a cyan "Visualize" button becomes available and opens the Surface Deformation Visualizer app (Figure 8a). When the visualizer is opened, the app (i) reprojects the deformation-velocity file from radar to geographic coordinates, (ii) creates a velocity KML file for visualization in Google Earth, (iii) reprojects the deformation time-series files from radar to geographic coordinates, (iv) loads the full time series into memory, and (v) generates an interactive deformation-velocity map within the application. The interactive deformation-velocity map supports zooming and panning and allows users to click any location to view the corresponding deformation time series (Figure 8b). The app also provides options to download the time-series plot as a PNG image and to export the corresponding data as a CSV file. Users can generate time series either for a single point by entering coordinates or clicking a location, or for multiple points by delineating a polygon using Polygon Mode (Figure 8c). When a polygon is defined, time series are generated for all pixels within the polygon, and the corresponding PNG and CSV files are exported automatically.

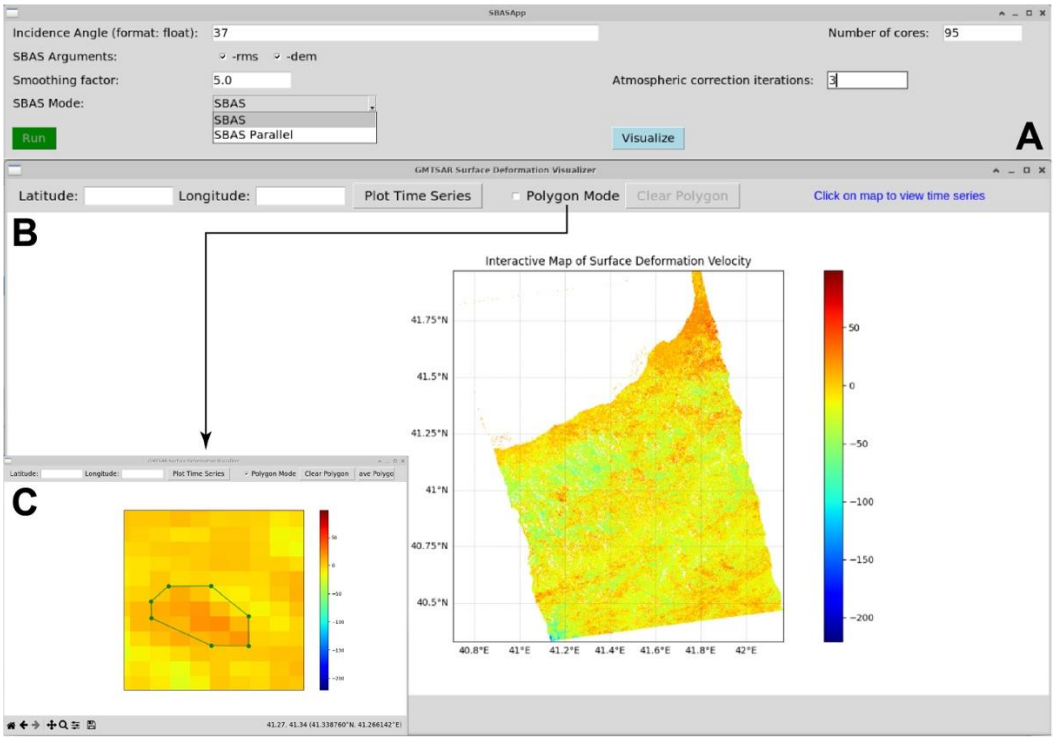

Figure 8: Panels demonstrating the required inputs for (a) SBAS inversion, (b) the Surface Deformation Visualizer app, and (c) Polygon Mode, which allows users to generate deformation time series for a manually delineated polygonal area.

We present the mean line-of-sight velocity (V_{LOS}) map derived using the processing workflow described above for the investigated landslide area (Figure 9a–b). The results show that V_{LOS} reaches up to 25 mm yr^{-1} around the landslide source area. We extracted a deformation time series near the landslide crown, where the surface deformation exhibits

a noticeable increase in November and culminates in hillslope failure approximately one month later, on 8 December 2025 (Figure 9c).

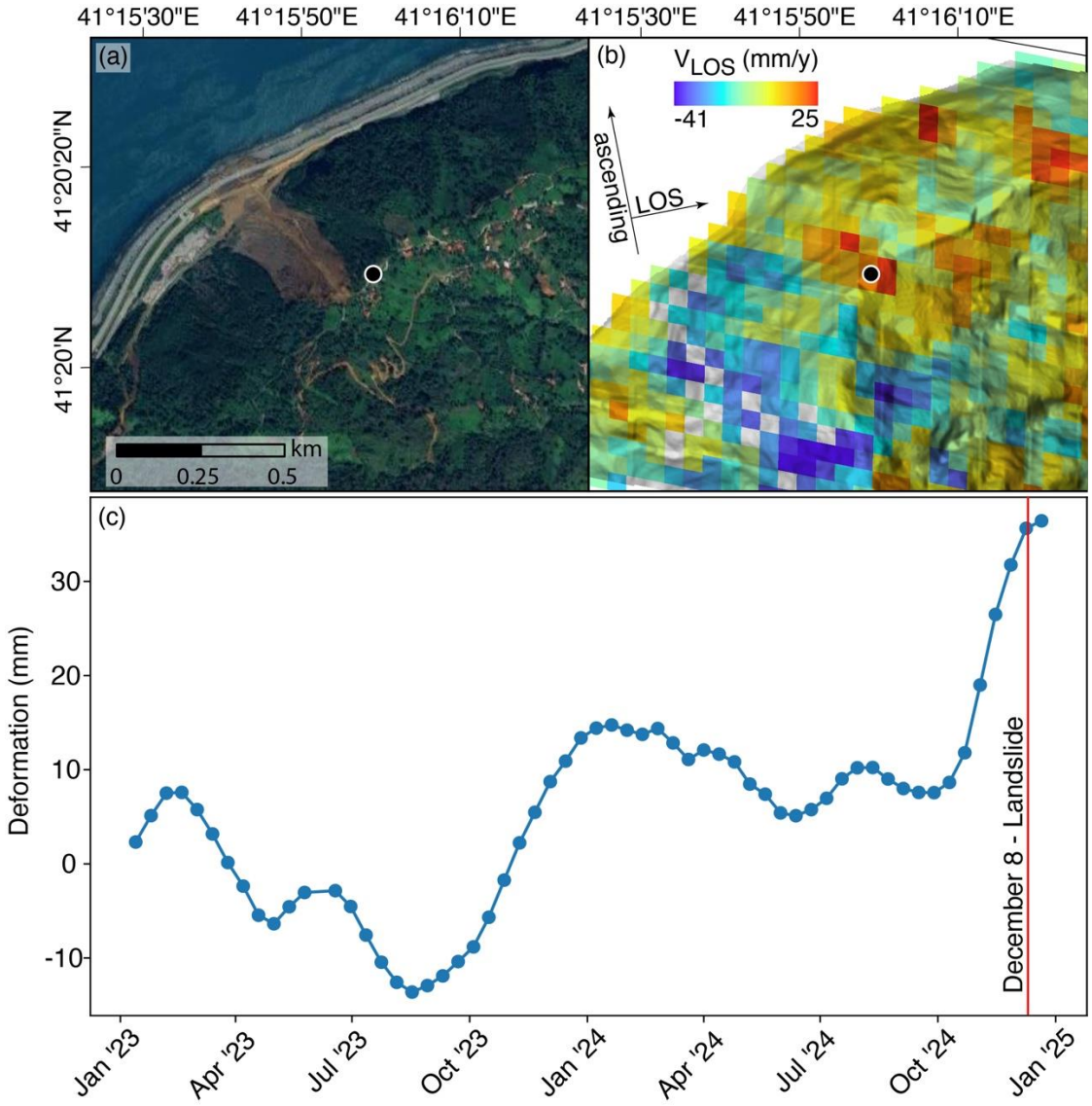

Figure 9: (a) Map of the Güngören landslide (failure on 8 December 2024). (b) Mean annual line-of-sight velocity (V_{LOS}) map derived from the processing workflow described in the text. (c) Example deformation time series from the location indicated in (b), illustrating the precursory deformation captured prior to collapse. The Google Earth image in (a) depicts post-landslide conditions on 20 May 2025.

3. Discussion

While InSARLite improves usability compared to command-line and Python-based alternatives such as Jupyter notebooks, the current release has certain limitations due to both internal design choices and external dependencies.

It supports time series analysis exclusively using Sentinel-1 SLC images acquired in IW mode. This focus allows for streamlined alignment with one of the most widely used data formats, but it excludes other acquisition modes and sensors supported by GMTSAR. The tool processes data at the subswath level and does not yet support burst-wise processing, which has recently become available via the ASF. Although InSARLite automates DEM handling, it is currently limited to a small set of sources, namely SRTM 30 m and 90 m, which restricts flexibility. It also does not currently allow users to specify a fixed phase jump for unwrapping, a feature that can be important critical for accurate coseismic deformation analysis.

Despite being a processing intensive task, any parallelization approach for coregistering images relative to the master image is not integrated. Additionally, the tool does not provide intuitive ways to visualize intermediate outputs, such as interferograms, at various processing stages. Time series analysis is restricted to SBAS, with no alternative approaches such as PSI currently available. The tool does not support estimation of three-dimensional (3D) displacement fields using both ascending and descending satellite passes, nor does it facilitate multi-sensor fusion for deformation analysis, such as combining Sentinel-1 data with ALOS-2 or TerraSAR-X.

To address these limitations and further enhance the tool's capabilities, several improvements could be implemented. These include support for multi-sensor and multi-satellite time series analysis through data fusion and harmonization. The interface could also be extended with an intuitive and scalable environment for bulk visualization of interferograms and other intermediate products to facilitate manual quality control. The capability to estimate 3D displacement by combining ascending and descending track data can also be implemented. Moreover, alternative time series approaches beyond SBAS, such as PSI, can be integrated into the given pipeline.

To improve quality control, several automated checks can be incorporated. These include assessments of pixel eligibility for SB inversion based on reliable unwrapped data counts, spatio-temporal coherence consistency, loop closure error detection, and phase bridging for unwrapping error correction. Additional methods can evaluate interferogram quality based on coherence and coverage metrics, residual RMS errors during SB inversion, and filtering or deramping of final time series outputs. Finally, the tool can explore the integration of parallelization strategies for image co-registration, such as those proposed by Romano and Lapegna (2021), to further increase processing efficiency. The open-source nature of InSARLite can facilitate these developments by enabling collaborative contributions from the community.

4. Conclusions

This study presents InSARLite, a fully open-source and user-friendly graphical interface designed to automate and simplify the GMTSAR-based InSAR time-series workflow. By structuring the process into four guided stages, from project configuration through interferogram generation, unwrapping, and SBAS inversion, InSARLite substantially reduces the technical overhead typically required for InSAR processing. The tool integrates features such as automated data querying and downloading, DEM handling, master selection, interferogram network design, optional atmospheric correction, intuitive mask creation, and an interactive environment for visualizing deformation time series. These enhancements enable end-to-end time-series analysis with minimal reliance on command-line scripting while preserving user control over key processing choices.

Application of InSARLite to the 8 December 2024 Güngören landslide in northeastern Türkiye demonstrates the tool's capability to support rapid geohazard assessment. The workflow efficiently processed a multi-year Sentinel-1 archive and enabled interactive inspection of both spatial and temporal deformation patterns. Although detailed geomorphic interpretation is beyond the scope of this technical contribution, the case study shows how InSARLite can be used to evaluate possible precursory deformation by combining systematic time-series visualization with targeted interrogation of slope-scale signals. This example highlights the value of an accessible, modular processing environment for supporting post-event investigations and exploring deformation indicators relevant to early-warning frameworks.

While the current release focuses on Sentinel-1 IW mode and SBAS inversion, it provides a robust and extensible foundation for deformation monitoring. Planned developments include support for burst-wise processing, ionospheric correction, multi-sensor data ingestion, alternative time-series methods such as Persistent Scatterer Interferometry, and enhanced tools for intermediate-stage visualization and automated quality control. Implementing these improvements will broaden the tool's applicability across diverse geophysical contexts and strengthen its role in operational and scientific workflows.

By bridging the gap between raw SAR data and interpretable deformation products through an intuitive and streamlined interface, InSARLite aims to broaden access to InSAR-based hazard assessment.

Code availability section

Name of the code/library: The source codes of InSARLite are available via data repository:

https://doi.org/10.5281/zenodo.17210560

Hardware requirements: The installation requirements for GMTSAR also apply to InSARLite (https://github.com/gmtsar/gmtsar). Beyond this minimum configuration, we tested InSARLite on two different systems:

High-End

Operating System: Ubuntu 20.04.4 LTS

Processor:

- Dual-socket Intel® Xeon® Gold 6248R CPUs @ 3.00 GHz
- 96 logical CPUs (48 physical cores, 2 threads per core)
- CPU max frequency: 4.0 GHz
- L1 Cache: 1.5 MiB, L2 Cache: 48 MiB, L3 Cache: 71.5 MiB

Memory: 1.5 TiB DDR4 RAM

Storage: ~200 TiB across multiple drives including high-capacity volumes and SSDs (e.g., 18.2 TiB × 8, 7 TiB × 7)

Low-End

Operating System: Ubuntu 24.04.1 LTS

Processor:

- 12th Gen Intel® Core™ i7-12700H
- 14 physical cores, 20 logical threads
- Maximum clock speed: 2.3 GHz

Memory: 32 GiB DDR5 RAM (2 × 16 GiB modules @ 4800 MHz)

Storage: 2.0 TiB + 1.0 TiB NVMe SSDs

GPU: Integrated Nvidia T600 & Intel® IRIS® Xe Graphics

Program language: Python 3.8+

Software required: GMTSAR

Program size: 414KB

Authorship contribution statement

Muhammad Badar Munir: Conceptualization, Software, Methodology, Formal analysis, Visualization, Writing - review & editing. Hakan Tanyas: Supervision, Resources, Investigation, Visualization, Writing -review & editing. Islam Fadel: Software, Methodology, Investigation, Review & editing. Ling Chang: Supervision, Investigation,

Review & editing. Amira Zaki: Methodology, Formal analysis, Review & editing. Ashok Dahal: Software, Review & editing. Cees van Westen: Supervision, Investigation, Review & editing. Serkan Girgin: Software, Investigation, Review & editing.

References

Ansari, H., Zan, F. D., Adam, N., Goel, K., & Bamler, R. (2016, 10-15 July 2016). Sequential estimator for distributed scatterer interferometry. 2016 IEEE International Geoscience and Remote Sensing Symposium (IGARSS),

Bekaert, D. P. S., Handwerger, A. L., Agram, P., & Kirschbaum, D. B. (2020). InSAR-based detection method for mapping and monitoring slow-moving landslides in remote regions with steep and mountainous terrain: An application to Nepal. *Remote Sensing of Environment*, *249*, 111983. https://doi.org/https://doi.org/10.1016/j.rse.2020.111983

Berardino, P., Fornaro, G., Lanari, R., & Sansosti, E. (2002). A new algorithm for surface deformation monitoring based on small baseline differential SAR interferograms. *IEEE Transactions on Geoscience and Remote Sensing*, *40*(11), 2375-2383.

Biggs, J., & Wright, T. J. (2020). How satellite InSAR has grown from opportunistic science to routine monitoring over the last decade. *Nature Communications*, *11*(1), 3863. https://doi.org/10.1038/s41467-020-17587-6

Bürgmann, R., Rosen, P. A., & Fielding, E. J. (2000). Synthetic Aperture Radar Interferometry to Measure Earth's Surface Topography and Its Deformation. *Annual Review of Earth and Planetary Sciences*, *28*(Volume 28, 2000), 169-209. https://doi.org/https://doi.org/10.1146/annurev.earth.28.1.169

Calò, F. (2012, 22-27 July 2012). DORIS project: The European downstream service for landslides and subsidence risk management. 2012 IEEE International Geoscience and Remote Sensing Symposium,

Camacho, A. G., Fernández, J., & Cannavò, F. (2018). PAF: A software tool to estimate free-geometry extended bodies of anomalous pressure from surface deformation data. *Computers & Geosciences*, *111*, 235-243. https://doi.org/https://doi.org/10.1016/j.cageo.2017.11.014

Chen, Y., Remy, D., Froger, J.-L., Peltier, A., Villeneuve, N., Darrozes, J., Perfettini, H., & Bonvalot, S. (2017). Long-term ground displacement observations using InSAR and GNSS at Piton de la Fournaise volcano between 2009 and 2014. *Remote Sensing of Environment*, *194*, 230-247. https://doi.org/https://doi.org/10.1016/j.rse.2017.03.038

Cigna, F., & Tapete, D. (2021). Present-day land subsidence rates, surface faulting hazard and risk in Mexico City with 2014–2020 Sentinel-1 IW InSAR. *Remote Sensing of Environment*, *253*, 112161. https://doi.org/https://doi.org/10.1016/j.rse.2020.112161

Costantini, M., Minati, F., Trillo, F., Ferretti, A., Novali, F., Passera, E., Dehls, J., Larsen, Y., Marinkovic, P., Eineder, M., Brcic, R., Siegmund, R., Kotzerke, P., Probeck, M., Kenyeres, A., Proietti, S., Solari, L., & Andersen, H. S. (2021, 11-16 July 2021). European Ground Motion Service (EGMS). 2021 IEEE International Geoscience and Remote Sensing Symposium IGARSS,

Ferretti, A., Prati, C., & Rocca, F. (2001). Permanent scatterers in SAR interferometry. *IEEE Transactions on Geoscience and Remote Sensing*, *39*(1), 8-20. https://doi.org/10.1109/36.898661

Ghorbani, Z., Khosravi, A., Maghsoudi, Y., Mojtahedi, F. F., Javadnia, E., & Nazari, A. (2022). Use of InSAR data for measuring land subsidence induced by groundwater withdrawal and climate change in Ardabil Plain, Iran. *Scientific Reports*, *12*(1), 13998. https://doi.org/10.1038/s41598-022-17438-y

Gorum, T., Yılmaz, A., Tanyas, H., Akgun, A., Fidan, S., Akbaş, A., Karabacak, F., Coşkun, S., Uçar, T., Kılıcasan, H., & Tatar, O. (2025). *8 Aralık 2024 Güngören, Arhavi (Artvin) Moloz Çığının Oluşum Dinamiği ve Alanın Heyelan Tehlike ve Risk Bakımından Değerlendirmesi*. https://doi.org/10.5281/zenodo.14625940

Gurrola, E., Rosen, P., Sacco, g. f., Zebker, H., Simons, M., & Sandwell, D. (2010). InSAR Scientific Computing Environment. *AGU Fall Meeting Abstracts*.

Haghshenas Haghighi, M., & Motagh, M. (2019). Ground surface response to continuous compaction of aquifer system in Tehran, Iran: Results from a long-term multi-sensor InSAR analysis. *Remote Sensing of Environment*, *221*, 534-550. https://doi.org/https://doi.org/10.1016/j.rse.2018.11.003

He, K., Lombardo, L., Chang, L., Sadhasivam, N., Hu, X., Fang, Z., Dahal, A., Fadel, I., Luo, G., & Tanyas, H. (2024). Investigating earthquake legacy effect on hillslope deformation using InSAR-derived time series. *Earth Surface Processes and Landforms*, *49*(3), 980-990. https://doi.org/https://doi.org/10.1002/esp.5746

Hooper, A. (2008). A multi-temporal InSAR method incorporating both persistent scatterer and small baseline approaches. *Geophysical Research Letters, 35, 2008 ; doi:10.1029/2008GL034654*, *35*. https://doi.org/10.1029/2008GL034654

Hrysiewicz, A., Wang, X., & Holohan, E. P. (2023). EZ-InSAR: An easy-to-use open-source toolbox for mapping ground surface deformation using satellite interferometric synthetic aperture radar. *Earth Science Informatics*, *16*(2), 1929-1945. https://doi.org/10.1007/s12145-023-00973-1

Jin, Z., & Fialko, Y. (2021). Coseismic and Early Postseismic Deformation Due to the 2021 M7.4 Maduo (China) Earthquake. *Geophysical Research Letters*, *48*(21), e2021GL095213. https://doi.org/https://doi.org/10.1029/2021GL095213

Khorrami, M., Abrishami, S., Maghsoudi, Y., Alizadeh, B., & Perissin, D. (2020). Extreme subsidence in a populated city (Mashhad) detected by PSInSAR considering groundwater withdrawal and geotechnical properties. *Scientific Reports*, *10*(1), 11357. https://doi.org/10.1038/s41598-020-67989-1

Kim, J.-W., Lu, Z., & Kaufmann, J. (2019). Evolution of sinkholes over Wink, Texas, observed by high-resolution optical and SAR imagery. *Remote Sensing of Environment*, *222*, 119-132.

Lanari, R., Casu, F., Manzo, M., Zeni, G., Berardino, P., Manunta, M., & Pepe, A. (2007). An overview of the Small BAseline Subset algorithm: A DInSAR technique for surface deformation analysis [Review]. *Pure and Applied Geophysics*, *164*(4), 637-661. https://doi.org/10.1007/s00024-007-0192-9

Lee, S. J., & Chae, S. H. (2024, 15-18 Dec. 2024). Development of KARI-MT-InSAR Tool for Highly-Efficient Surface Deformation Monitoring Using Large-Scale SAR Data. 2024 IEEE International Conference on Big Data (BigData),

Liu, G. X., Ding, X. L., Li, Z. L., Li, Z. W., Chen, Y. Q., & Yu, S. B. (2004). Pre- and co-seismic ground deformations of the 1999 Chi-Chi, Taiwan earthquake, measured with SAR interferometry. *Computers & Geosciences*, *30*(4), 333-343. https://doi.org/https://doi.org/10.1016/j.cageo.2003.08.011

Lu, Z., Kwoun, O., & Rykhus, R. (2007). Interferometric Synthetic Aperture Radar (InSAR): Its Past, Present and Future. *Photogrammetric Engineering and Remote Sensing*, *73*.

Meyer, F. J., Hogenson, K., Kennedy, J. H., Lewandowski, A. F., Albright, R. W., Short, G., Flores-Anderson, A. I., & Rosen, P. A. (2025). Facilitating the Golden Age of Synthetic Aperture Radar: New tools, services, and training to make synthetic aperture radar data more accessible. *IEEE Geoscience and Remote Sensing Magazine*, 2-13. https://doi.org/10.1109/MGRS.2025.3526588

Morishita, Y., Lazecky, M., Wright, T. J., Weiss, J. R., Elliott, J. R., & Hooper, A. (2020). LiCSBAS: An Open-Source InSAR Time Series Analysis Package Integrated with the LiCSAR Automated Sentinel-1 InSAR Processor. *Remote Sensing*, *12*(3).

Motagh, M., & Riedel, B. (2024). Editorial for Special Issue: RADAR REMOTE SENSING. *PFG – Journal of Photogrammetry, Remote Sensing and Geoinformation Science*, *92*(3), 211-211. https://doi.org/10.1007/s41064-024-00293-z

Pasquali, P., Atzori, S., Cantone, A., Riccardi, P., De Filippi, M., & Barbieri, M. (2012). SARscape®, a Commercial-Off-The-Shelf Software Package for the Measurement, Monitoring and Modeling of Geophysical Phenomena. https://doi.org/https://doi.org/10.3997/2214-4609.20143070

Pavez, A., Remy, D., Bonvalot, S., Diament, M., Gabalda, G., Froger, J.-L., Julien, P., Legrand, D., & Moisset, D. (2006). Insight into ground deformations at Lascar volcano (Chile) from SAR interferometry, photogrammetry and GPS data: Implications on volcano dynamics and future space monitoring. *Remote Sensing of Environment*, *100*(3), 307-320.

Romano, D., & Lapegna, M. (2021). A GPU-Parallel Image Coregistration Algorithm for InSar Processing at the Edge. *Sensors (Basel)*, *21*(17). https://doi.org/10.3390/s21175916

Sadhasivam, N., Chang, L., & Tanyaş, H. (2024). An integrated approach for mapping slow-moving hillslopes and characterizing their activity using InSAR, slope units and a novel 2-D deformation scheme. *Natural Hazards*, *120*(4), 3919-3941. https://doi.org/10.1007/s11069-023-06353-8

Samsonov, S., Dille, A., Dewitte, O., Kervyn, F., & d'Oreye, N. (2020). Satellite interferometry for mapping surface deformation time series in one, two and three dimensions: A new method illustrated on a slow-moving landslide. *Engineering Geology*, *266*, 105471. https://doi.org/https://doi.org/10.1016/j.enggeo.2019.105471

Sandwell, D., Mellors, R., Tong, X., Xu, X., Wei, M., & Wessel, P. (2011). *GMTSAR: An InSAR Processing System Based on Generic Mapping Tools (Second Edition)*.

Talib, O. C., Shimon, W., Sarah, K., & Tonian, R. (2022). Detection of sinkhole activity in West-Central Florida using InSAR time series observations. *Remote Sensing of Environment*, *269*, 112793.

Tong, X., & Schmidt, D. (2016). Active movement of the Cascade landslide complex in Washington from a coherence-based InSAR time series method. *Remote Sensing of Environment*, *186*, 405-415. https://doi.org/https://doi.org/10.1016/j.rse.2016.09.008

Torres, R., Snoeij, P., Geudtner, D., Bibby, D., Davidson, M., Attema, E., Potin, P., Rommen, B., Floury, N., Brown, M., Traver, I. N., Deghaye, P., Duesmann, B., Rosich, B., Miranda, N., Bruno, C., L'Abbate, M., Croci, R., Pietropaolo, A.,…Rostan, F. (2012). GMES Sentinel-1 mission. *Remote Sensing of Environment*, *120*, 9-24. https://doi.org/https://doi.org/10.1016/j.rse.2011.05.028

Wang, Y., Zhu, X. X., & Bamler, R. (2012). Retrieval of phase history parameters from distributed scatterers in urban areas using very high resolution SAR data. *ISPRS Journal of Photogrammetry and Remote Sensing*, *73*, 89-99. https://doi.org/https://doi.org/10.1016/j.isprsjprs.2012.06.007

Wang, Z., Guo, L., Gong, H., Li, X., Zhu, L., Sun, Y., Chen, B., & Zhu, X. (2023). Land subsidence simulation based on Extremely Randomized Trees combined with Monte Carlo algorithm. *Computers & Geosciences*, *178*, 105415. https://doi.org/https://doi.org/10.1016/j.cageo.2023.105415

Wegnüller, U., Werner, C., Strozzi, T., Wiesmann, A., Frey, O., & Santoro, M. (2016). Sentinel-1 Support in the GAMMA Software. *Procedia Computer Science*, *100*, 1305-1312. https://doi.org/https://doi.org/10.1016/j.procs.2016.09.246

Weiss, J. R., Walters, R. J., Morishita, Y., Wright, T. J., Lazecky, M., Wang, H., Hussain, E., Hooper, A. J., Elliott, J. R., Rollins, C., Yu, C., González, P. J., Spaans, K., Li, Z., & Parsons, B. (2020). High-Resolution Surface Velocities and Strain for Anatolia From Sentinel-1 InSAR and GNSS Data. *Geophysical Research Letters*, *47*(17), e2020GL087376. https://doi.org/https://doi.org/10.1029/2020GL087376

Xu, X., Sandwell, D. T., Tymofyeyeva, E., González-Ortega, A., & Tong, X. (2017). Tectonic and Anthropogenic Deformation at the Cerro Prieto Geothermal Step-Over Revealed by Sentinel-1A InSAR. *IEEE Transactions on Geoscience and Remote Sensing*, *55*(9), 5284-5292. https://doi.org/10.1109/TGRS.2017.2704593

Yu, C., Li, Z., & Penna, N. T. (2018). Interferometric synthetic aperture radar atmospheric correction using a GPS-based iterative tropospheric decomposition model. *Remote Sensing of Environment*, *204*, 109-121. https://doi.org/https://doi.org/10.1016/j.rse.2017.10.038

Yu, C., Li, Z., Penna, N. T., & Crippa, P. (2018). Generic Atmospheric Correction Model for Interferometric Synthetic Aperture Radar Observations. *Journal of Geophysical Research: Solid Earth*, *123*(10), 9202-9222. https://doi.org/https://doi.org/10.1029/2017JB015305

Yu, C., Penna, N. T., & Li, Z. (2017). Generation of real-time mode high-resolution water vapor fields from GPS observations. *Journal of Geophysical Research: Atmospheres*, *122*(3), 2008-2025. https://doi.org/https://doi.org/10.1002/2016JD025753

Yu, Y., Balz, T., Luo, H., Liao, M., & Zhang, L. (2019). GPU accelerated interferometric SAR processing for Sentinel-1 TOPS data. *Comput. Geosci.*, *129*(C), 12–25. https://doi.org/10.1016/j.cageo.2019.04.010

Yunjun, Z., Fattahi, H., & Amelung, F. (2019). Small baseline InSAR time series analysis: Unwrapping error correction and noise reduction. *Computers & Geosciences*, *133*, 104331. https://doi.org/https://doi.org/10.1016/j.cageo.2019.104331

Zaki, A., Chang, L., Manzella, I., Meijde, M. v. d., Girgin, S., Tanyas, H., & Fadel, I. (2024). Automated Python workflow for generating Sentinel-1 PSI and SBAS interferometric stacks using SNAP on Geospatial Computing Platform. *Environmental Modelling & Software*, *178*, 106075. https://doi.org/https://doi.org/10.1016/j.envsoft.2024.106075

Zebker, H. A., & Villasenor, J. (1992). Decorrelation in interferometric radar echoes. *IEEE Transactions on Geoscience and Remote Sensing*, *30*(5), 950-959. https://doi.org/10.1109/36.175330

Zhao, C., Lu, Z., Zhang, Q., & de la Fuente, J. (2012). Large-area landslide detection and monitoring with ALOS/PALSAR imagery data over Northern California and Southern Oregon, USA. *Remote Sensing of Environment*, *124*, 348-359. https://doi.org/https://doi.org/10.1016/j.rse.2012.05.025

Zuhlke, M., Fomferra, N., Brockmann, C., Peters, M., Veci, L., Malik, J., & Regner, P. (2015, December 01, 2015). SNAP (Sentinel Application Platform) and the ESA Sentinel 3 Toolbox. Sentinel-3 for Science Workshop, Venice, Italy.

List of Figures